

# MODELING POROUS DUST GRAINS WITH BALLISTIC AGGREGATES. II. LIGHT SCATTERING PROPERTIES

YUE SHEN, B. T. DRAINE, AND ERIC T. JOHNSON

Princeton University Observatory, Princeton, NJ 08544, USA

Received 2009 January 14; accepted 2009 February 26; published 2009 April 28

## ABSTRACT

We study the light scattering properties of random ballistic aggregates constructed in Shen et al. Using the discrete-dipole approximation, we compute the scattering phase function and linear polarization for random aggregates with various sizes and porosities, and with two different compositions: 100% silicate and 50% silicate +50% graphite. We investigate the dependence of light scattering properties on wavelength, cluster size, and porosity using these aggregate models. We find that while the shape of the phase function depends mainly on the size parameter of the aggregates, the linear polarization depends on both the size parameter and the porosity of the aggregates, with increasing degree of polarization as the porosity increases. Contrary to previous studies, we argue that the monomer size has negligible effects on the light scattering properties of ballistic aggregates, as long as the constituent monomer is smaller than the incident wavelength up to  $2\pi a_0/\lambda \sim 1.6$  where  $a_0$  is the monomer radius. Previous claims for such monomer size effects are in fact the combined effects of size parameter and porosity. Finally, we present aggregate models that can reproduce the phase function and polarization of scattered light from the AU Mic debris disk and from cometary dust, including the negative polarization observed for comets at scattering angles  $160^\circ \lesssim \theta < 180^\circ$ . These aggregates have moderate porosities,  $\mathcal{P} \approx 0.6$ , and are of sub- $\mu\text{m}$  size for the debris disk case, or  $\mu\text{m}$  size for the comet case.

*Key words:* circumstellar matter – comets: general – dust, extinction – interplanetary medium – polarization – scattering – stars: individual (AU Mic, GJ 803)

*Online-only material:* color figures

## 1. INTRODUCTION

Interplanetary dust particles (IDPs) collected in the Earth’s stratosphere by high-flying aircraft (Brownlee 1985; Warren et al. 1994) usually have irregular shapes and fluffy structures. Similar structures have been produced in laboratory and microgravity experiments of dust particle interactions (Wurm & Blum 1998; Blum & Wurm 2000; Krause & Blum 2004). It has also been suggested that interstellar dust grains may consist primarily of such aggregate structures (e.g., Mathis & Whiffen 1989; Dorschner & Henning 1995), with a mixture of various chemical compositions and vacuum.

Porous, composite aggregates are often modeled as a cluster of small spheres (“spherules” or “monomers”), assembled under various aggregation rules. The optical properties of these aggregates can be calculated using numerical schemes such as the generalized multisphere Mie (GMM) solution (Mackowski 1991; Xu 1997) or the discrete dipole approximation (DDA) method (e.g., Purcell & Pennypacker 1973; Draine & Flatau 1994). These methods have been used to study the optical properties of different kinds of aggregates during the past decade (e.g., West 1991; Lumme & Rahola 1994; Petrova et al. 2000; Kimura et al. 2006; Bertini et al. 2007; Lasue et al. 2009); most of those studies are dedicated to interpret the phase function and polarization of light scattered by cometary dust.

In a companion paper (Shen et al. 2008, hereafter Paper I), we constructed aggregates using three specific aggregation rules: ballistic agglomeration (BA), ballistic agglomeration with one migration (BAM1), and ballistic agglomeration with two migrations (BAM2). We developed a set of parameters to characterize the irregular structure of these aggregates. While the BA clusters are essentially the Ballistic Particle-Cluster Agglomeration (BPCA) clusters frequently used in the literature (e.g., West 1991; Kozasa et al. 1992, 1993; Ossenkopf

1993; Kimura et al. 2006; Bertini et al. 2007; Lasue et al. 2009), the newly introduced BAM1 and BAM2 clusters have geometries that are random but substantially less “fluffy” than the BA clusters. The effective porosity  $\mathcal{P}$  (Equation (12) in Paper I) increases from BAM2→BAM1→BA and covers a wide dynamical range, allowing us to investigate the effects of porosity on the optical properties of the aggregates in a systematic way. Using these aggregation rules, we can construct grain models with various sizes and compositions. In Paper I, we computed total scattering and absorption cross sections for the three types of aggregates (BA, BAM1, and BAM2), for three different compositions (50% silicate and 50% graphite; 50% silicate and 50% amorphous carbon AC1, Rouleau & Martin 1991, and 100% silicate), and for wavelengths from 0.1  $\mu\text{m}$  to 4  $\mu\text{m}$ . The purpose of this paper is to investigate the detailed light scattering properties of these aggregates, i.e., the phase function and the linear polarization.

The paper is organized as follows: in Section 2 we recapitulate our aggregate models; the scattering phase function and linear polarization for various ballistic aggregates are presented in Section 3, where we explore the dependence of light scattering properties on aggregate properties; we present examples of aggregates that can be applied to circumstellar debris disks and cometary dust in Section 4, and we show that moderate porosity aggregates can reproduce the observed scattering and polarization properties of dust in both solar system comets and extrasolar debris disks. We summarize our results in Section 5.

## 2. AGGREGATE MODELS

A detailed description of the target generation algorithms and resulting geometric properties of the BA, BAM1, and BAM2 clusters can be found in Paper I. Here we review some of the basic concepts that will be used in the following sections.

**Table 1**  
Cluster Geometries

Cluster	$\mathcal{P}$	$R/a_{\text{eff}}$	$N_{\text{dip}}$	$n_{\text{dip}}$	Figures
BA.256.1	0.8598	1.9249	115656	451.8	6
BA.256.2	0.8525	1.8925	105855	413.5	6
BA.256.3	0.8553	1.9050	102725	401.3	6
BAM1.32.4	0.6188	1.3791	13903	434.5	4ab
BAM1.256.1	0.7060	1.5038	103921	405.9	6
BAM1.256.2	0.7412	1.5693	107160	418.6	6
BAM1.256.3	0.6980	1.4904	107047	418.2	6
BAM2.256.1	0.5632	1.3179	113696	444.1	1, 3, 4cd, 5, 6, 7
BAM2.256.2	0.5781	1.3333	103509	404.3	1, 3, 4cd, 5, 6, 7
BAM2.256.3	0.5818	1.3372	107332	419.3	1, 3, 4cd, 5, 6, 7
BAM2.512.14	0.6127	1.3719	211211	412.5	4ab
BAM2.1024.1	0.6386	1.4039	414977	405.3	4cd, 8
BAM2.1024.2	0.6476	1.4158	412077	402.4	4cd, 8
BAM2.1024.3	0.6387	1.4041	430184	420.1	4cd, 8

**Note.** Naming convention: “BA.256.1” means realization 1 of the  $N = 256$  BA clusters.

Each aggregate is composed of  $N$  spherical monomers with radius  $a_0$ . We define the “effective radius” of a cluster,  $a_{\text{eff}}$ , to be the radius of an equal-volume solid sphere; thus our aggregates have

$$a_{\text{eff}} = N^{1/3} a_0. \quad (1)$$

The structure of the cluster is characterized by a porosity parameter  $\mathcal{P}$  (see Equation (12) of Paper I) and a characteristic radius  $R \equiv a_{\text{eff}}/(1 - \mathcal{P})^{1/3}$  (see Equation (11) of Paper I), which depends on  $\mathcal{P}$  and is typically 1–2 times  $a_{\text{eff}}$ . Tables 1 and 2 of Paper I give tabulated mean values of  $\mathcal{P}$  and  $R/a_{\text{eff}}$  for the three types of aggregates with  $2^3 \leq N \leq 2^{16}$ . For a given value of  $N$ , the BA clusters have the highest  $\mathcal{P}$ , while the BAM2 clusters have the lowest  $\mathcal{P}$ . Information for the specific cluster geometries employed in this paper can be found in Table 1, including the porosity  $\mathcal{P}$ , the number  $N_{\text{dip}}$  of dipoles representing the realization, and the number of dipoles per sphere,  $n_{\text{dip}} = N_{\text{dip}}/N$ . The actual geometry (including images) of these and other realizations of BA, BAM1, and BAM2 clusters can be obtained online.<sup>1</sup>

In Paper I, we considered three different compositions: 50% silicate + 50% graphite, 50% silicate + 50% AC1, and 100% silicate. Silicate material accounts for perhaps 2/3 of the total mass of interstellar dust, and it is natural to assume that silicates will also provide the bulk of the refractory material in comets or debris disks. Interstellar silicates are amorphous; and amorphous silicates are believed to dominate the silicate mass even in the case of comets or circumstellar disks where crystalline silicates have been detected. We use the “astrosilicate” dielectric function (Draine & Lee 1984; Draine 2003).

Carbonaceous material provides a significant fraction of the total mass of interstellar grains, and this may also be true of dust in comets and debris disks. The smallest carbonaceous particles in the ISM consist primarily of polycyclic aromatic hydrocarbon material, but the form of the carbon in the larger grains (where most of the carbon resides) remains uncertain: Pendleton & Allamandola (2002) conclude that the hydrocarbon material is  $\sim 85\%$  aromatic (ring-like) and  $15\%$  aliphatic (chain-like), but Dartois et al. (2004) claim that aliphatic material predominates, with at most  $15\%$  of the carbon in aromatic form. To explore the effect of material that is strongly absorptive in the visible,

we use the dielectric tensor of graphite for the carbon in our mixed-composition aggregates.

In the present paper, we study the scattering properties of aggregates with two compositions: 100% silicate, or 50% silicate + 50% graphite (volume fractions). In Paper I, we found that aggregates consisting of 50% silicate + 50% AC1 amorphous carbon had scattering properties intermediate between the 100% silicate and 50% silicate + 50% graphite aggregates.

Calculations are performed using DDSCAT version 7.0 (Draine & Flatau 2008). DDSCAT is a code based on the discrete dipole approximation (Purcell & Pennypacker 1973; Draine & Flatau 1994), designed to compute scattering and absorption of electromagnetic waves by targets with arbitrary geometry and composition, for targets that are not too large compared to the wavelength  $\lambda$ . For each cluster type (defined by  $N$ , aggregation rule, and composition) we generally average over three random realizations and 54 orientations for each realization.<sup>2</sup> DDSCAT 7.0 allows us to treat the graphite monomers as randomly oriented spheres with the anisotropic dielectric tensor of graphite.

### 3. SCATTERING PHASE FUNCTION AND POLARIZATION

The phase function and linear polarization of the scattered light as functions of scattering angle  $\theta$  can be retrieved from the elements of the  $4 \times 4$  Muller matrix  $S_{ij}$  (e.g., Bohren & Huffman 1983). For unpolarized incident light, the scattered light phase function is proportional to  $S_{11} = (4\pi^2/\lambda^2) dC_{\text{sca}}/d\Omega$  (where  $dC_{\text{sca}}/d\Omega$  is the differential scattering cross section for unpolarized incident light) and the linear polarization parameter is  $p = -S_{21}/S_{11}$ . By definition, the polarization is perpendicular/parallel to the scattering plane when  $p$  is positive/negative.

We have obtained  $S_{11}(\theta)$  and  $p(\theta)$  for our realization- and orientation-averaged aggregates for wavelengths  $0.1 \leq \lambda/\mu\text{m} \leq 4$ , and show representative examples in Figures 1–6. For illustrative purposes, in most cases we will present the results for the BAM2 aggregates—the aggregate geometry with the lowest porosity. Orientation-averaged scattering properties for the clusters studied in this paper (including wavelengths not shown in the figures) are available online.<sup>3</sup>

#### 3.1. Wavelength Dependence

We first show the wavelength dependence of  $S_{11}$  and linear polarization for  $N = 256$ -monomer BAM2 clusters with monomer radius  $a_0 = 0.02 \mu\text{m}$  in Figure 1, for selected wavelengths. For the  $N = 256$  BAM2 case,  $a_{\text{eff}} = 0.127 \mu\text{m}$ , the porosity  $\mathcal{P} \approx 0.58$  (see Table 1), and the characteristic radius  $R \approx 1.334a_{\text{eff}} = 0.17 \mu\text{m}$ . The phase function shows a relatively smooth dependence on wavelength  $\lambda$ : for  $\lambda \lesssim 0.5 \mu\text{m}$  ( $x \equiv 2\pi R/\lambda > 2$ ), it shows a strong peak in the forward scattering and a mild backscattering enhancement, with the overall forward–backward asymmetry decreasing monotonically as the incident wavelength increases. For linear polarization, the situation is more complicated. The polarization near  $\theta \approx 90^\circ$  first decreases as  $\lambda$  increases, reaches a minimum at  $\lambda \approx R$ , and then rises again with increasing  $\lambda$ , approaching  $p(90^\circ) = 100\%$  in the Rayleigh limit. The wavelength  $\lambda_{\text{min,pol}}$

<sup>2</sup> Nine values of the angle  $\Theta$  between the cluster principal axis  $\hat{\mathbf{a}}_1$  and  $\hat{\mathbf{x}}$  (the direction of the incident light), and 6 values of the rotation angle  $\beta$  of the cluster around  $\hat{\mathbf{a}}_1$ . We use a single value of the rotation angle  $\Phi$  of  $\hat{\mathbf{a}}_1$  around  $\hat{\mathbf{x}}$  because we average over four scattering planes.

<sup>3</sup> <http://www.astro.princeton.edu/~draine/SDJ2009.html>

<sup>1</sup> <http://www.astro.princeton.edu/~draine/agglom.html>

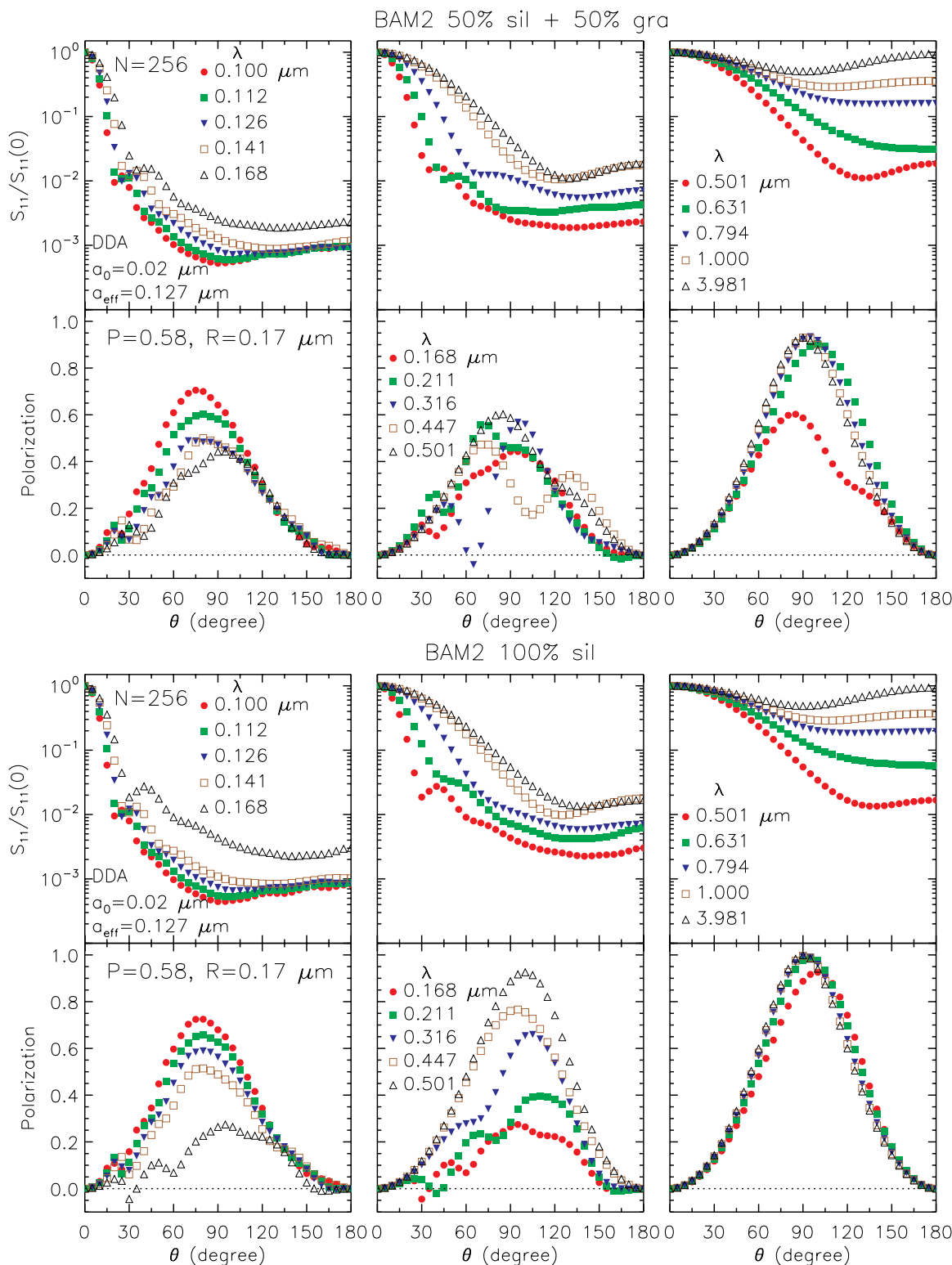


**Figure 1.** Wavelength dependence of  $S_{11}$  (normalized using  $S_{11}(0)$ ) and polarization for the  $N = 256$  and  $a_0 = 0.02 \mu\text{m}$  BAM2 clusters for two compositions, averaged over three realizations (BAM2.256.1-3) and 54 random orientations for each realization. Upper: the silicate-graphite case; bottom: the 100% silicate case. (A color version of this figure is available in the online journal.)

where  $p(90^\circ)$  is minimum is well defined for the pure silicate, with  $\lambda_{\text{min.pol}} \approx 0.17 \mu\text{m}$ . For the graphite-silicate composition it is less well defined, with minima near  $\sim 0.17 \mu\text{m}$  and  $\sim 0.45 \mu\text{m}$ . The increase of polarization with increasing wavelength in the optical band is known as the polarization color effect in cometary scattered light observations (e.g., Chernova

et al. 1996; Levasseur-Regourd & Hadancik 2001). The reverse behavior of increasing polarization with decreasing wavelength in the UV band, however, is more complicated to interpret. It could be caused by the change in the size parameter  $x \equiv 2\pi R/\lambda$ , or changes in the dielectric function as  $\lambda$  varies, or both. We will return to this point in Section 3.3.

It was shown in Paper I that the EMT-Mie model provides a good approximation for the total extinction cross section as a function of  $\lambda$ , provided that the vacuum fraction  $f_{\text{vac}}$  is set to  $f_{\text{vac}} \approx \mathcal{P}$ . We now test to see if the EMT-Mie model reproduces the scattering phase function  $S_{11}(\theta)$  and polarization  $p(\theta)$ . For the EMT-Mie calculations we use an optimal value of the vacuum fraction  $f_{\text{vac}} = 0.55$  and the same amount of solid material as in the  $N = 256$  BAM2 clusters. For the effective dielectric permittivity  $\epsilon_{\text{eff}}$  we use the Bruggeman rule (see Bohren & Huffman 1983)

$$\sum_i f_i \frac{\epsilon_i - \epsilon_{\text{eff}}}{\epsilon_i + 2\epsilon_{\text{eff}}} = 0, \quad (2)$$

where  $f_i$  and  $\epsilon_i$  are the volume fraction and dielectric permittivity of each composition, including vacuum. There is always only one solution of  $\epsilon_{\text{eff}}$  that is physically meaningful. For graphite, we make the usual  $\frac{1}{3} - \frac{2}{3}$  approximation, and take  $\epsilon = \epsilon(E \parallel c)$  for  $f = \frac{1}{3}f_{\text{graphite}}$ ,  $\epsilon = \epsilon(E \perp c)$  for  $f = \frac{2}{3}f_{\text{graphite}}$ .

The EMT-Mie results are shown in Figure 2 for the silicate-graphite and the pure silicate cases, in parallel to Figure 1. The EMT calculations at a fixed wavelength show resonances that arise from the use of spheres, but these should be smoothed out when modeling nonspherical particles, which are randomly oriented and will not show such well-defined resonances. Therefore, we have smoothed the EMT results using a Gaussian kernel

$$\tilde{S}_{ij} = \frac{\int d \ln a \exp[-[\ln(a/\bar{a})]^2/2\sigma^2] S_{ij}(a)}{\int d \ln a \exp[-[\ln(a/\bar{a})]^2/2\sigma^2]}, \quad (3)$$

where  $\sigma = \bar{a}/(\bar{a} + \lambda/2\pi)$  and  $\bar{a} = (1 - f_{\text{vac}})^{-1/3} a_{\text{eff}}$  is the radius of the Mie sphere. The phase function and polarization are then computed using the smoothed  $\tilde{S}_{ij}$ .

By directly comparing Figures 1 and 2, it is evident that the EMT-Mie results for  $S_{11}(\theta)$  and linear polarization  $p(\theta)$  do share the same trends we see in the DDA calculations. Nevertheless, there are substantial differences between the EMT-Mie results and our DDA results. One obvious feature is that the EMT-Mie model tends to underestimate the backscattering for short wavelength ( $\lambda \lesssim 0.6 \mu\text{m}$ ,  $x \gtrsim 1.8$ ), a feature already revealed by the behavior of the asymmetry parameter  $g \equiv \langle \cos \theta \rangle$  discussed in Paper I (Figure 12). For example, consider the forward-backward asymmetry  $S_{11}(0)/S_{11}(180^\circ)$  for  $\lambda = 0.168 \mu\text{m}$ : the DDA calculations for the mixed graphite-silicate BAM2 cluster give  $\sim 450$ , while the EMT-Mie calculation gives  $\sim 7000$ .

To compare the EMT-Mie results and our DDA calculations in detail we plot the relative differences in Figure 3, for the silicate plus graphite case (upper) and the pure silicate case (bottom). The difference can be substantial for specific wavelengths or scattering angles. For example, for  $\theta \approx 90^\circ$  scattering at  $\lambda \approx 0.50 \mu\text{m}$ , the EMT-Mie calculation underestimates the polarization by a factor  $\sim 2$ , for both the graphite-silicate clusters and the pure silicate clusters. Although Paper I showed that EMT-Mie calculations can be used to obtain moderately accurate total extinction and scattering cross sections, Figure 3 shows that the scattering phase function and polarization estimated using EMT-Mie calculations do not accurately reproduce the scattering properties of irregular clusters.

### 3.2. Does Monomer Size Matter?

There is another parameter that might affect  $S_{11}$  and polarization: the monomer size. There have been claims that

large monomer size is crucial in decreasing the polarization and in producing the negative polarization branch observed in cometary dust (e.g., Petrova et al. 2000; Bertini et al. 2007). However, in these previous studies, variations in monomer size were always coupled with changes in porosity  $\mathcal{P}$  and cluster size  $R$ ; hence effects attributed to varying the monomer size may in fact be due to variations in  $\mathcal{P}$  or  $R$ . We have already seen in Paper I that the apparent effects of monomer size on total cross sections are essentially the effects of varying  $\mathcal{P}$  or  $R$ .

To isolate the effect of monomer size, we compare clusters with the same  $a_{\text{eff}}$  and very similar  $\mathcal{P}$  (thus  $R$  is also comparable), but different monomer size  $a_0$ . Thus the effect of monomer size, if there is any, is decoupled from other effects. We first consider the same example used in Figure 8 of Paper I: the  $N = 32$  BAM1 cluster realization BAM1.32.4 ( $\mathcal{P} = 0.619$ ,  $R/a_{\text{eff}} = 1.379$ ) with monomer size  $a_0 = 0.0504 \mu\text{m}$  and the  $N = 512$  BAM2 cluster realization BAM2.512.14 ( $\mathcal{P} = 0.613$ ,  $R/a_{\text{eff}} = 1.372$ ) with  $a_0 = 0.02 \mu\text{m}$ . Both clusters have  $a_{\text{eff}} = 0.160 \mu\text{m}$  and  $R = 0.220 \mu\text{m}$ . The orientation-averaged results are shown in Figures 4(a) and (b) for two wavelengths and for the silicate-graphite composition only. Although there are slight differences, the two cases have similar phase functions and polarizations: at constant  $R$  and  $\mathcal{P}$ , varying the monomer size  $a_0$  had little effect on the phase function and polarization.

The above example employed moderate-sized clusters ( $x = 2\pi R/\lambda \lesssim 3.9$ ) composed of small monomers ( $2\pi a_0/\lambda \lesssim 0.9$ ). Figures 4(c) and (d) compare the scattering properties of two large clusters ( $R \approx 1.4 \mu\text{m}$ ,  $x = 11.1$  and  $13.9$ ) with similar porosities  $\mathcal{P} \approx 0.6$  but different monomer sizes. For  $\lambda = 0.631 \mu\text{m}$  and  $0.794 \mu\text{m}$ , clusters with  $a_0 = 0.10 \mu\text{m}$  and  $0.16 \mu\text{m}$  show similar (though not identical because of the slight difference in porosity of the two clusters; see Section 3.4) polarization  $p(\theta)$ , despite the substantial difference in monomer size. Therefore we conclude that monomer size is immaterial as long as the monomer size is smaller than the incident wavelength up to  $2\pi a_0/\lambda \sim 1.6$ .

### 3.3. Dependence on Cluster Size

As we have discussed in Section 3.1 for fixed-size clusters, the dependence of the phase function and linear polarization on wavelength  $\lambda$  is likely to be caused by the changes in both the size parameter and dielectric function. To investigate the effects of cluster size at fixed incident wavelength (i.e., the effects of the size parameter alone), we use  $N = 256$ , BAM2 clusters with monomer size  $a_0 = 0.02, 0.025, 0.03 \mu\text{m}$ , or  $R \sim 0.169, 0.212, 0.254 \mu\text{m}$ . These clusters have the same porosity, and as argued in the previous section, the monomer size has negligible effects, hence any difference must be caused by changes in  $R$ . The results are shown in Figure 5 for both compositions. We present results at two wavelengths:  $\lambda = 0.126 \mu\text{m}$  ( $< R$ ) and  $\lambda = 0.631 \mu\text{m}$  ( $> R$ ). In both cases the backward/forward scattering asymmetry increases with increasing the size parameter  $2\pi R/\lambda$ .

In general, we expect  $p(90^\circ) \rightarrow 1$  in the Rayleigh scattering limit  $R/\lambda \ll 1$ , with the peak polarization decreasing with increasing  $R/\lambda$ . This decline with increasing  $R/\lambda$  is seen in Figures 5(b) and (d). However, the results in Figures 5(a) and (c) show that the variation in  $p_{\text{max}}$  with increasing  $R$  is not monotonic: at  $\lambda = 0.126 \mu\text{m}$  when  $R \gtrsim \lambda$  and when the dielectric function is very absorptive, for both the 100% silicate and 50% silicate + 50% graphite  $N = 256$  BAM2 clusters, the polarization is an increasing function of  $R$  over the range



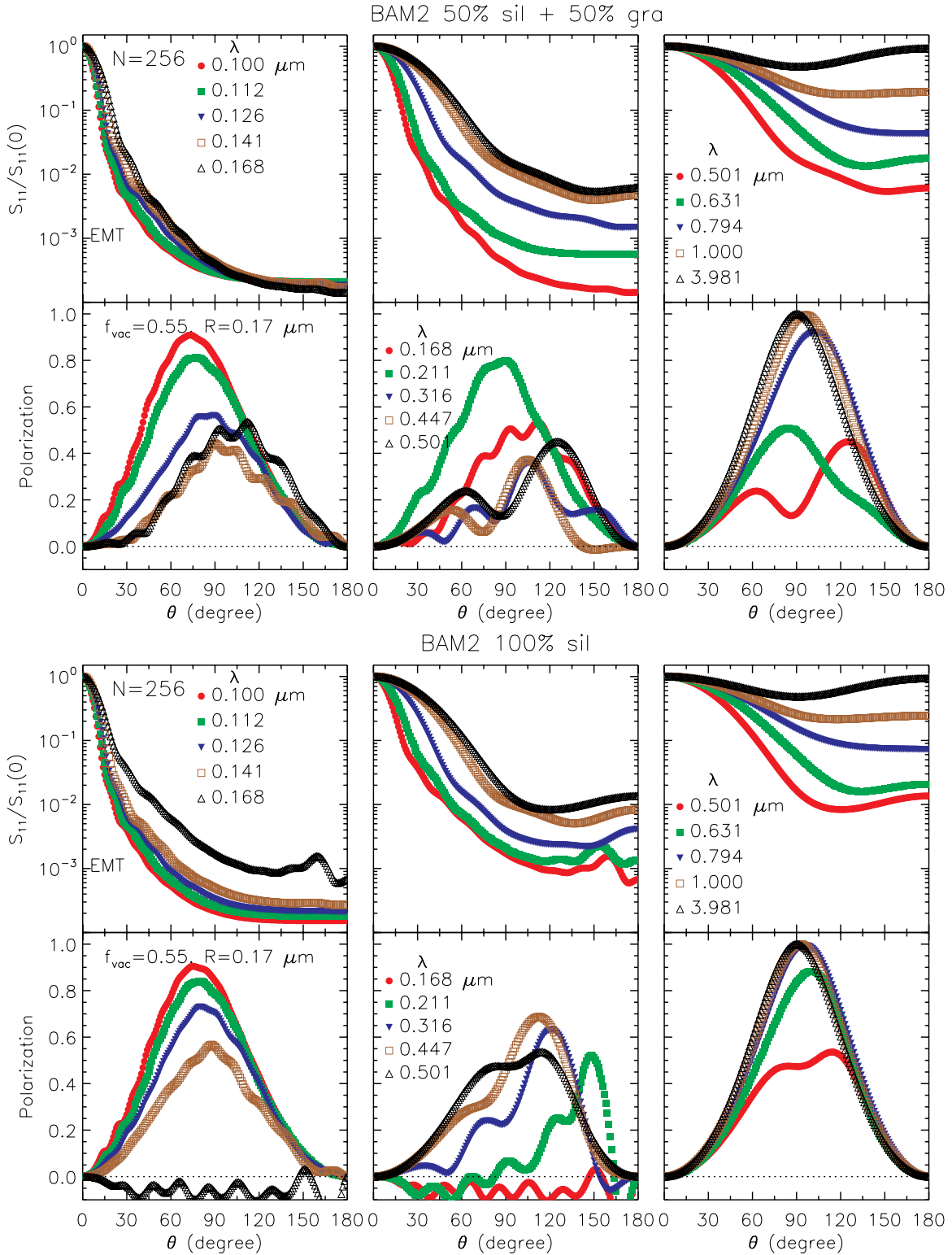


**Figure 2.** Same as Figure 1, but for the EMT-Mie results (smoothed as in Equation (3)) computed for  $f_{\text{vac}} = 0.55$  and the same amount of solid material as in the  $N = 256$  BAM2 clusters in Figure 1.

(A color version of this figure is available in the online journal.)

$1.3 \lesssim R/\lambda \lesssim 2$ . Thus for these cases the polarization at  $\lambda = 0.126 \mu\text{m}$  has a minimum at some size  $R_{\text{crit}} < 1.3\lambda$ .

However, the dependence of polarization on  $R/\lambda$  depends on the dielectric function (and therefore on both composition and wavelength). For  $\lambda = 0.631 \mu\text{m}$  the 100% silicate BAM2 clusters with  $\mathcal{P} \approx 0.6$  have the polarization declining with

increasing  $R$  out to  $R/\lambda = 2.2$  (the largest value computed, see Section 4.2 and Figures 7(d) and 8)—without showing a reversal in the polarization behavior. The situation is even more complicated for the silicate plus graphite case, where there is no coherent trend when  $R \approx \lambda$  (see Figures 1(a), 7(a), and 7(b)). Based on the cases investigated thus far, it appears that

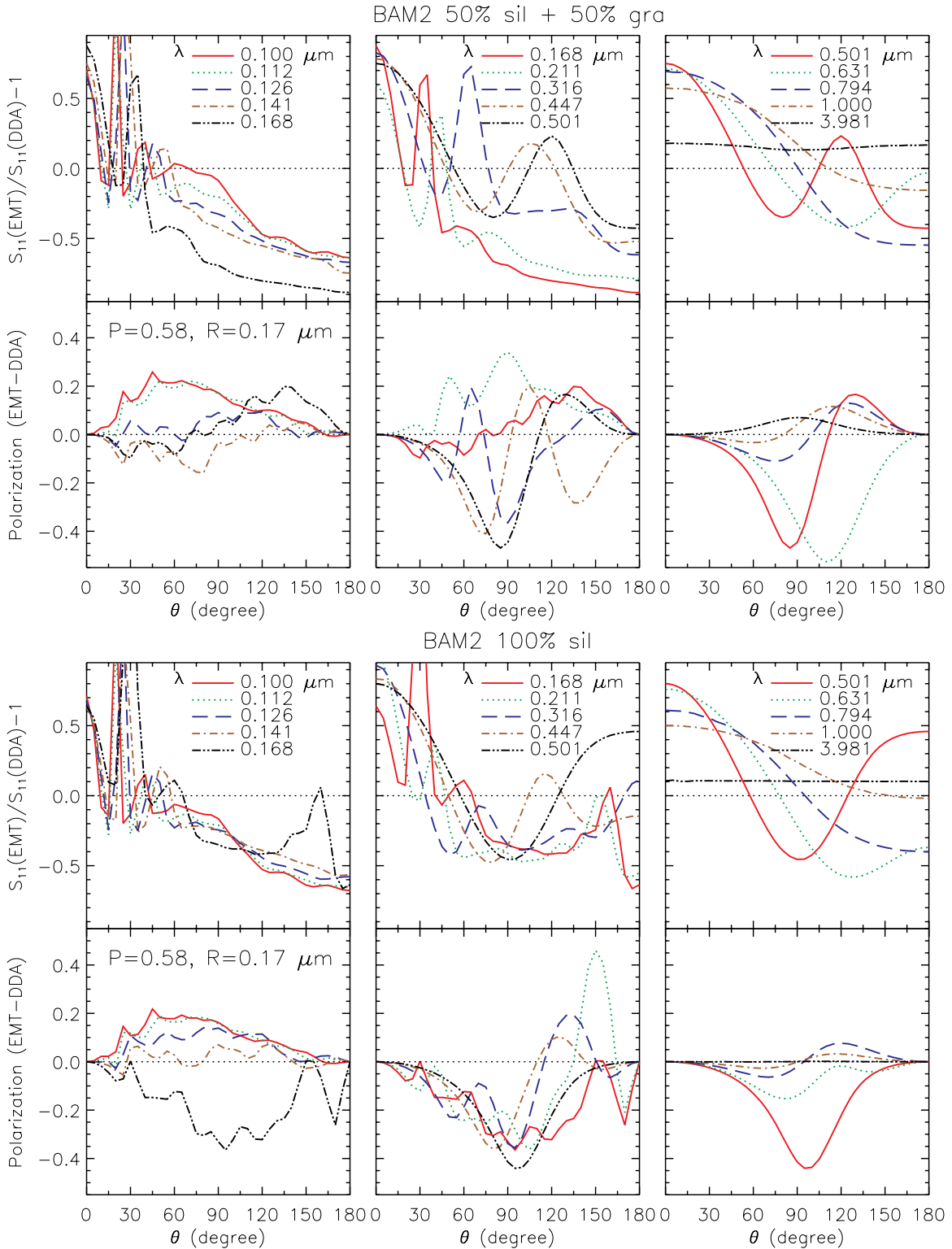


**Figure 3.** Difference in the phase function and polarization for the DDA results for the  $N = 256$  BAM2 clusters from Figure 1 and EMT results from Figure 2. (A color version of this figure is available in the online journal.)

when the dielectric function has only weak absorption (e.g., 100% astrosilicate at  $\lambda = 0.631 \mu\text{m}$ ), for fixed porosity  $\mathcal{P}$  the polarization is a monotonically decreasing function of cluster size  $R$  from the Rayleigh limit  $R \ll \lambda$  up to  $R/\lambda \lesssim 2$ . On the other hand, when the dielectric function is strongly absorptive (e.g., materials at  $\lambda = 0.126 \mu\text{m}$  or silicate-graphite clusters

at  $\lambda = 0.631 \mu\text{m}$ ), for fixed porosity the polarization declines with increasing  $R$  from the Rayleigh limit until it reaches a local minimum at  $R \approx \lambda$  (the transition is less distinct for the silicate-graphite case than for the pure silicate case), and then rises as  $R$  is further increased, at least out to  $R/\lambda \approx 2$  (e.g., Figures 5(a) and 7(a), (b)).

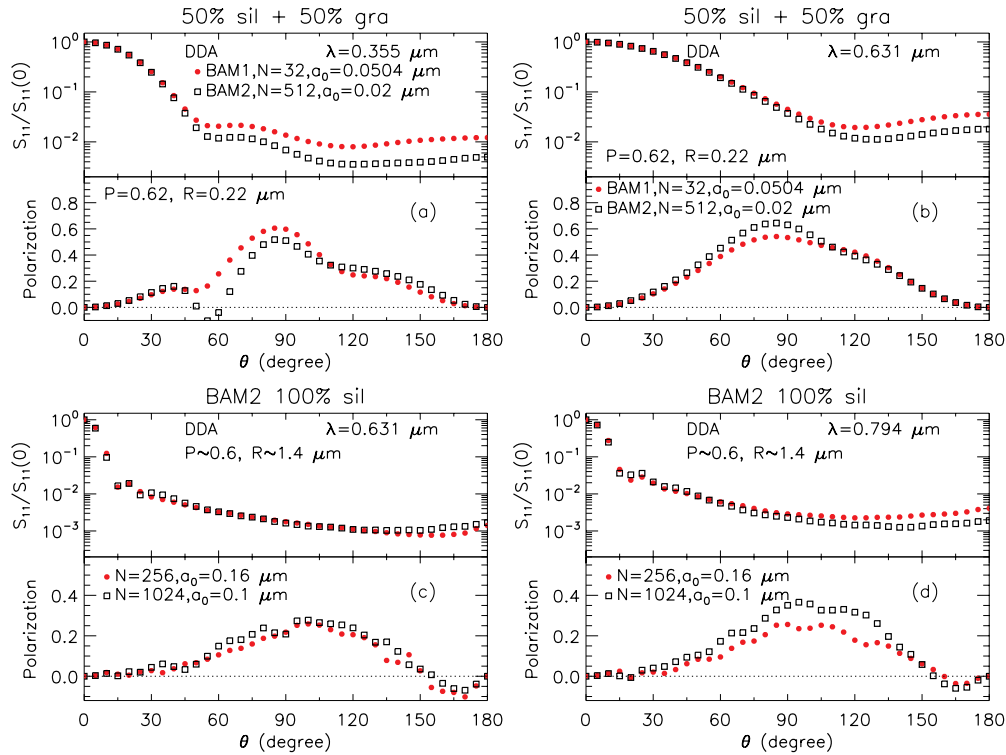


**Figure 4.** Tests for the effect of monomer size. (a) Comparable phase function and polarization for two silicate-graphite clusters—BAM1.32.4 and BAM2.512.14—with similar porosities  $\mathcal{P} \sim 0.619, 0.613$  and cluster size  $R \sim 0.221, 0.220 \mu\text{m}$ , but different monomer size  $a_0 = 0.0504, 0.02 \mu\text{m}$ , for  $\lambda = 0.355 \mu\text{m}$  ( $x \equiv 2\pi R/\lambda = 3.9$ ). (b) Same as (a), but for  $\lambda = 0.631 \mu\text{m}$  ( $x = 2.2$ ). (c) Comparable phase function and polarization at  $\lambda = 0.631 \mu\text{m}$  for two large silicate clusters with similar porosity  $\mathcal{P} \sim 0.57$  and  $0.64$ , and size  $R \sim 1.4 \mu\text{m}$  ( $x = 13.9$ ), but different monomer size  $a_0 = 0.10, 0.16 \mu\text{m}$  ( $2\pi a_0/\lambda = 1.0, 1.6$ ). (d) Same as (c), but for  $\lambda = 0.794 \mu\text{m}$ . The clusters in (c) and (d) are each represented by three realizations (BAM2.256.1-3 and BAM2.1024.1-3) and 54 orientations per realization. These four examples show that for fixed size  $R$  and porosity  $\mathcal{P}$ , the monomer size  $a_0$  is unimportant if  $2\pi a_0/\lambda < 1$ , and of only secondary importance even when  $2\pi a_0/\lambda \approx 1.6$ .

(A color version of this figure is available in the online journal.)

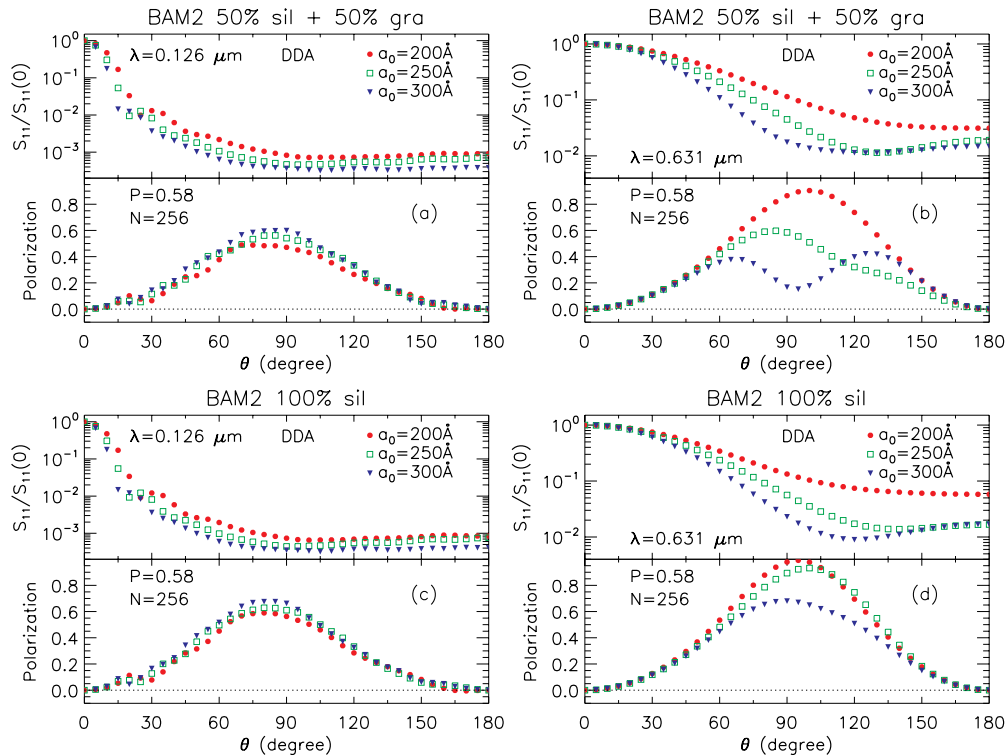


**Figure 5.** Cluster size dependence of  $S_{11}$  and polarization for  $N = 256$  BAM2 clusters with  $a_0 = 0.02, 0.025, 0.03 \mu\text{m}$ , for two compositions, averaged over three realizations (BAM2.256.1-3) and 54 random orientations. These clusters have typical sizes  $R \sim 0.169, 0.212, 0.254 \mu\text{m}$ , but same porosity  $\mathcal{P} \sim 0.58$ . Examples are shown at incident wavelength  $\lambda = 0.126 \mu\text{m} < R$  and  $0.631 \mu\text{m} > R$ .

(A color version of this figure is available in the online journal.)

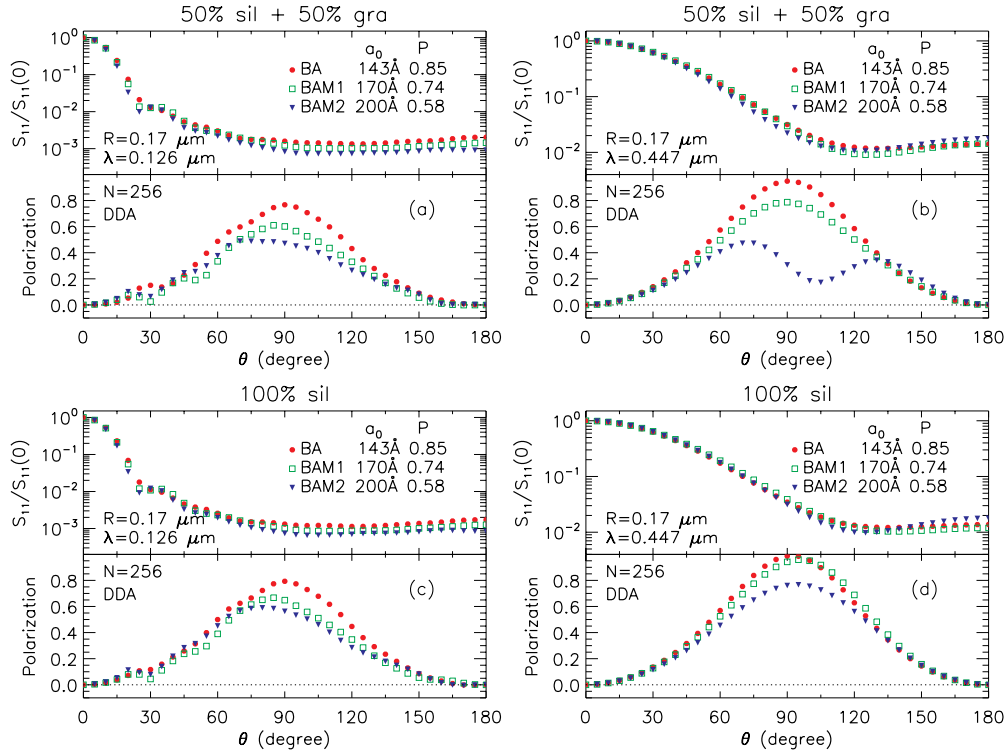


**Figure 6.** Effect of porosity on  $S_{11}$  and polarization for  $N = 256$  BA, BAM1, and BAM2 clusters which have the same cluster size  $R \sim 0.17 \mu\text{m}$  but different porosities  $P = 0.85, 0.74, 0.58$ , using three realizations per cluster (BA.256.1-3, BAM1.256.1-3, and BAM2.256.1-3) and 54 orientations per realization. (A color version of this figure is available in the online journal.)

### 3.4. Dependence on Porosity

We now investigate the effect of porosity on the scattering phase function and linear polarization. Previous studies on the porosity effect using only the BPCA and/or the even more porous “ballistic cluster-cluster agglomeration (BCCA)” clusters were quite limited in the dynamical range of porosity, and changes in porosity were coupled with changes in cluster size. To decouple from the cluster size effect we choose clusters with comparable sizes, but different porosities. We use  $N = 256$  BA, BAM1, and BAM2 clusters, with monomer size  $a_0 = 143, 170, 200 \text{ \AA}$  respectively; hence these clusters have comparable size  $R \sim 0.17 \mu\text{m}$ , but different porosities  $P = 0.85, 0.74, 0.58$ .

We consider two regimes:  $\lambda < R$  and  $\lambda > R$ . The results are shown in Figure 6 for two example wavelengths,  $\lambda = 0.126 \mu\text{m}$  and  $\lambda = 0.447 \mu\text{m}$ , and for the two compositions. It is evident that in both regimes, porosity has little effect on the shape of the phase function.<sup>4</sup> On the other hand, higher porosity tends to increase the linear polarization for both  $R > \lambda$  and  $R < \lambda$ .

Most of the cases shown in this section have large linear polarization fraction [ $p(90^\circ) \gtrsim 50\%$ ]. Cometary dust typically has  $p(90^\circ) \lesssim 40\%$  and a negative branch of polarization at scattering angle  $\sim 160^\circ\text{--}180^\circ$  (e.g., Levasseur-Regourd & Hadancik 2001), observed at optical wavelengths. From the results of Sections 3.1–3.4 we expect that, in general, a reduced peak polarization and appearance of a negative polarization branch for  $160 \lesssim \theta < 180^\circ$  can be obtained by (1) increasing the cluster size  $R$ , and (2) making the cluster more compact (lower porosity  $P$ ). Examples of ballistic aggregates that are

able to reproduce these cometary dust features will be presented in Section 4.2.

## 4. APPLICATIONS OF BALLISTIC AGGREGATES

The light scattering properties of our ballistic aggregates can be applied to various observations. Here we focus on debris disks and cometary dust, where single scattering dominates in the optically thin regime. We show examples of aggregates that can reproduce qualitative and quantitative features observed in the scattered light from the debris disk around AU Mic (Graham et al. 2007) and from cometary dust (e.g., Lumme & Rahola 1994; Petrova et al. 2000; Kimura et al. 2006; Lasue et al. 2009). Due to computational limits, we cannot probe a sufficiently large parameter space to claim that our models are unique; nor do we attempt to fit a sophisticated model to the observations of a specific comet. Nevertheless, our examples (in particular the moderate-porosity BAM2 clusters) nicely reproduce most of the features observed in light scattered by debris-disk dust and cometary dust.

### 4.1. Debris Disk around AU Mic

Polarization maps of the debris disk surrounding the nearby M star AU Microscopii have been obtained by Graham et al. (2007) using *Hubble Space Telescope* (HST) Advanced Camera for Surveys (ACS) in the F606W optical band ( $\lambda_c = 0.590 \mu\text{m}$ ,  $\Delta\lambda = 0.230 \mu\text{m}$ ). The scattered light is polarized perpendicular to the disk plane. Graham et al. (2007) adopted the form for the phase function introduced by Henyey & Greenstein (1940):

$$S_{11} = \frac{1}{4\pi} \frac{1 - g^2}{(1 + g^2 - 2g \cos \theta)^{3/2}}, \quad (4)$$

<sup>4</sup> The slight difference in  $S_{11}/S_{11}(0)$  is likely caused by the different geometry of the BA, BAM1, and BAM2 clusters.



assumed that the polarization versus scattering angle varies as

$$p(\theta) = -\frac{S_{21}}{S_{11}} = p_{\max} \frac{\sin^2 \theta}{1 + \cos^2 \theta}, \quad (5)$$

and simultaneously fitted the phase function and linear polarization as a function of scattering angle to the observational data, obtaining  $g \approx 0.68$  and  $p_{\max} \approx 0.53$ . Graham et al. (2007) suggest that very porous ( $\mathcal{P} \approx 0.91$ – $0.94$ )  $\mu\text{m}$ -sized spherical grains or aggregates can produce these features based on Mie theory and DDA calculations for BA clusters (Kimura et al. 2006).

Here we will show that random aggregates with a much lower porosity ( $\mathcal{P} \approx 0.6$ ) can, in fact, better fit the observations of the AU Mic debris disk. To reproduce the observed features, we require that the phase function and linear polarization are both close to the functions (4) and (5) with the best-fit values of  $g$  and  $p_{\max}$  found by Graham et al. (2007). In particular, the intensity of scattered light at  $\theta = 0^\circ$  should be approximately a factor of 150 larger than the intensity at  $\theta = 180^\circ$ , and the maximum polarization should be  $\approx 0.5$ , although  $p(\theta)$  need not necessarily peak at  $\theta = 90^\circ$ .

Dust grains in debris disks will have a distribution of sizes. Much of the interstellar grain mass can be approximated by a power-law size distribution  $dn/dR \propto R^{-\alpha}$  for  $R \lesssim 0.25 \mu\text{m}$  with  $\alpha \approx 3.5$  (Mathis et al. 1977). Size distributions with  $\alpha \approx 3.5$  can be obtained from models with coagulation and collisional fragmentation (Dohnanyi 1969; Tanaka et al. 1996; Weidenschilling 1997).

For modeling comets and debris disks, we will consider a size distribution  $dn/dR \propto R^{-3.5}$ . For a fixed porosity (i.e., a particular type of aggregate with a fixed  $N$ ), this size distribution is just  $dn/da_0 \propto a_0^{-3.5}$ , where  $a_0$  is the monomer size. Hence the averaged phase function  $S_{11}(\theta)$  and polarization are

$$\bar{S}_{11}(\theta) = \frac{\int_{a_{\min}}^{a_{\max}} da_0 (dn/da_0) S_{11}(a_0, \theta)}{\int_{a_{\min}}^{a_{\max}} da_0 (dn/da_0)}, \quad (6)$$

$$\bar{p}(\theta) = \frac{\int_{a_{\min}}^{a_{\max}} da_0 (dn/da_0) S_{11}(a_0, \theta) p(a_0, \theta)}{\int_{a_{\min}}^{a_{\max}} da_0 (dn/da_0) S_{11}(a_0, \theta)}, \quad (7)$$

where  $a_{\min}$  and  $a_{\max}$  are the minimum and maximum values of the monomer size in our size distribution.

We consider  $N = 256$  BAM2 clusters ( $\mathcal{P} = 0.58$ ), with  $a_0 = 0.02, 0.03, 0.04, 0.05, 0.06, 0.07, 0.08 \mu\text{m}$ , which correspond to  $R \approx 0.169, 0.254, 0.339, 0.424, 0.508, 0.593, 0.678 \mu\text{m}$ , respectively. We show the calculated phase function and polarization for each of these clusters (averaged over orientations and three realizations) in Figure 7, at two wavelengths  $\lambda = 0.501$  and  $0.631 \mu\text{m}$ . For comparison with the scattering properties inferred for the dust around AU Mic, we calculate  $\bar{S}_{11}(\theta)$  and polarization  $\bar{p}(\theta)$  averaged over a size distribution  $dn/dR \propto R^{-3.5}$  with  $a_{\min} = 0.015 \mu\text{m}$  and  $a_{\max} = 0.065 \mu\text{m}$  ( $R_{\min} = 0.127 \mu\text{m}$ ,  $R_{\max} = 0.551 \mu\text{m}$ ), which are shown as dashed lines. The best-fit Henyey–Greenstein phase function (4) and polarization fitting function (5) from Graham et al. (2007) are shown as solid black lines. We plot the comparison for both the silicate–graphite composition (upper panels) and the pure silicate composition (bottom panels).

As we can see from Figure 7, the size-averaged silicate–graphite clusters produce close matches to the Henyey–Greenstein model at these optical wavelengths for both the phase function and linear polarization. These clusters have porosity

$\mathcal{P} \approx 0.6$  and overall size  $R \sim 0.2$ – $0.5 \mu\text{m}$ , i.e., they are sub- $\mu\text{m}$ -sized clusters with moderate porosity.

As discussed in Section 3.4, increasing porosity will increase the polarization of scattered light. Our highest porosity clusters are those BA clusters, which are commonly used in the literature, referred to as “BPCA” clusters (e.g., West 1991; Kozasa et al. 1992, 1993; Ossenkopf 1993; Kimura et al. 2006; Bertini et al. 2007; Lasue et al. 2009). We found that if we replace the BAM2 clusters in Figure 7 with BA clusters with the same number of monomers and monomer sizes, we can reproduce similar phase function features but overpredict the polarization. This is already seen in Graham et al. (2007) (e.g., their Figure 8). Thus we conclude that compact BAM2 clusters fit the observations of AU Mic better than the more porous BA clusters that have been considered previously.

#### 4.2. Cometary Dust

The phase function and linear polarization of scattered light have been observed in a variety of comets. Though different comets show quantitative differences in the phase function and polarization, there are some common features:

1. The phase function shows strong forward scattering with a weak enhancement in the backscattering; the geometric albedo (defined as  $A \equiv (S_{11}[180^\circ]\lambda^2)/(4\pi G)$  where  $G \approx \pi R^2$  is the averaged geometric cross section of the grain) of backscattered light is less than 0.06 (e.g., Hanner & Newburn 1989).
2. The linear polarization  $p(\theta)$  is a bell-shaped curve as a function of scattering angle, with a typical maximum value of 10%–30% (Dobrovolsky et al. 1986; Levasseur-Regourd et al. 1996), although gas contamination in polarimetric measurements with wide-band filters might depolarize the observed scattered light (Kiselev et al. 2004).
3. Within the 4000–7000 Å window, the polarization increases with wavelength, which is the so-called polarization color effect (e.g., Chernova et al. 1996; Levasseur-Regourd & Hadancik 2001).
4. Many comets show a negative branch of polarization at scattering angle larger than  $150^\circ$ – $160^\circ$ , with a minimum of  $\gtrsim -2\%$  (e.g., Dollfus et al. 1988; Eaton et al. 1992).

Most of these features, in particular the negative polarization branch, have been successfully reproduced using various aggregates which differ in geometry, composition, and porosity (e.g., Lumme & Rahola 1994; Petrova et al. 2000; Kimura et al. 2006; Bertini et al. 2007; Lasue et al. 2009). The aggregates studied here are capable of producing all these features as well. In addition, we have demonstrated the effects of grain size and porosity, and pointed out that the monomer size effect claimed by previous authors is in fact due to changes in cluster size  $R$  and/or porosity  $\mathcal{P}$ . For example, in Petrova et al. (2000) and Bertini et al. (2007), the difference in the prominence of the negative branch is caused by the effect of grain size when they increase the monomer size for the same configuration/porosity.

The reason that those authors did not find a negative branch of polarization for small monomer size ( $a_0 \lesssim 0.1 \mu\text{m}$ ) and a moderate number of monomers (a few tens) is that computational limits prevented them from using a sufficient number of monomers. To test this, we have computed a few realizations of BAM2 clusters with  $N = 1024$ , composed of small monomers ( $a_0 = 0.08 \mu\text{m}$ ). The results are shown in Figure 8 for optical wavelength  $\lambda = 0.631 \mu\text{m}$ , where the negative branch is evident for both compositions (it is more prominent at the usually

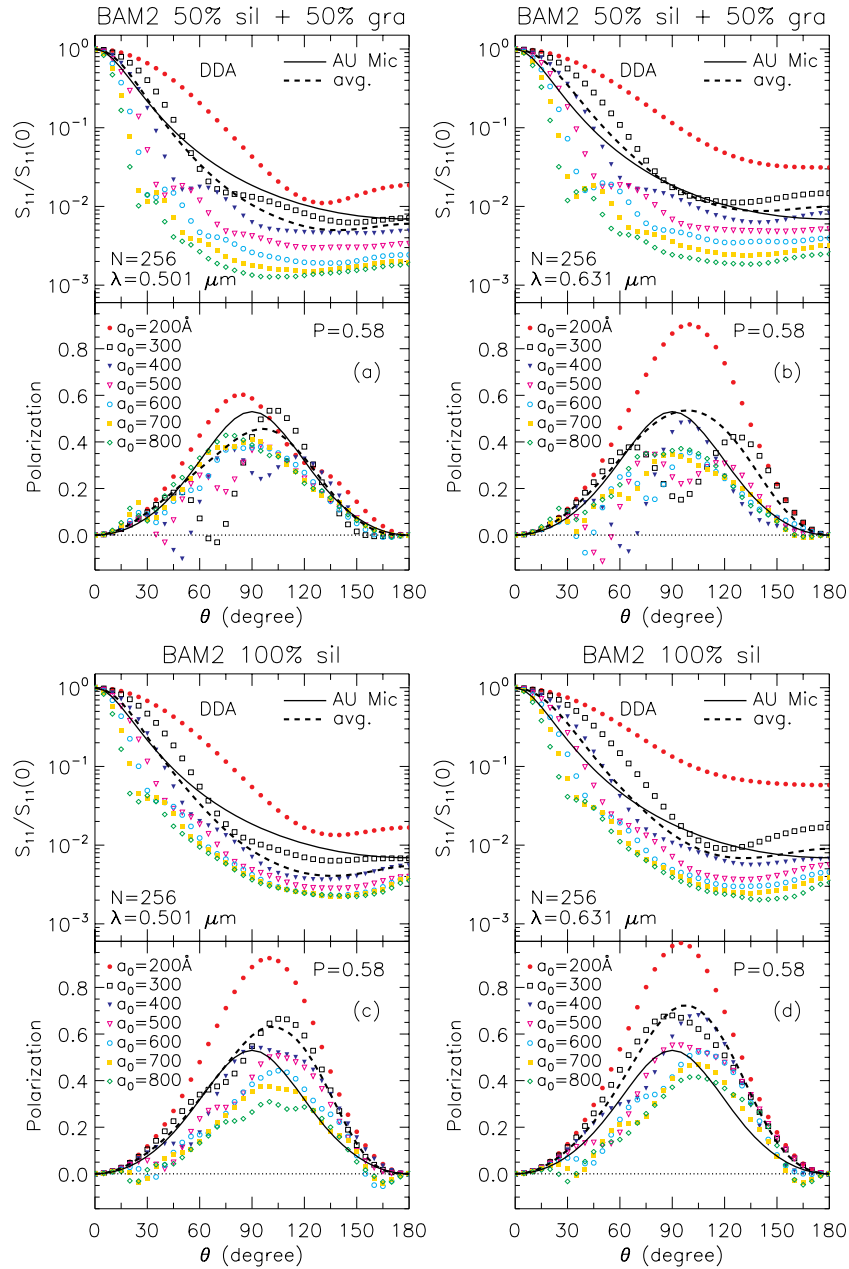


**Figure 7.** Applications to the debris disk around AU Mic. Scattering properties  $S_{11}(\theta)/S_{11}(0)$  and  $p(\theta)$  for three realizations of  $N = 256$  BAM2 clusters (BAM2.256.1-3), 54 orientations per realization, with monomer sizes  $a_0$  ranging from 200 Å to 800 Å ( $R$  from 0.169  $\mu\text{m}$  to 0.678  $\mu\text{m}$ ). Dashed lines show scattering properties obtained by averaging over a size distribution  $dn/dR \propto R^{-3.5}$  running from  $R_{\min} = 0.127 \mu\text{m}$  to  $R_{\max} = 0.551 \mu\text{m}$  (see text). Solid curves show phase function and polarization inferred by Graham et al. (2007) for an assumed angular dependence given by Equations (4) and (5). The adopted size distribution provides a good fit using clusters with porosity  $\mathcal{P} \approx 0.6$  and sizes  $R \approx 0.13\text{--}0.55 \mu\text{m}$ . For comparison, we also show results for clusters with  $a_0 = 700, 800 \text{ Å}$ , which exhibit the negative polarization branch observed in comets. Scattering properties are available at <http://www.astro.princeton.edu/~draine/SDJ2009.html>.

(A color version of this figure is available in the online journal.)

observed red band  $\lambda = 0.55 \mu\text{m}$ ). In Figure 8, we have also computed for the  $N = 1024$  BAM2 clusters using monomer size  $a_0 = 0.1 \mu\text{m}$ , shown as open squares; the dashed lines are the average of the results of the two monomer sizes, for a size distribution  $dn/dR \propto R^{-3.5}$  running from  $R_{\min} = 0.98 \mu\text{m}$  to  $R_{\max} = 1.54 \mu\text{m}$ .

These clusters are  $\mu\text{m}$ -size grains, which is consistent with the values found by other authors (e.g., Lumme & Rahola 1994; Petrova et al. 2000; Kimura et al. 2006), although the exact values depend on composition as well as porosity. We find that the  $N = 1024$ ,  $a_0 = 0.08, 0.1 \mu\text{m}$  BAM2 clusters composed of silicate and graphite (Figure 8(a)) with

$R \approx 1.1\text{--}1.4 \mu\text{m}$  and  $\mathcal{P} \approx 0.6$ , reproduce a backscattering albedo  $A = [S_{11}(180^\circ)\lambda^2]/(4\pi^2 R^2) \sim 0.04$  and a small negative polarization for scattering angles  $\sim 155^\circ\text{--}180^\circ$  peaking at ( $\sim -1\%$ ), representative of the typical values found in cometary observations, although the maximum polarization ( $\sim 45\%$ ) is a little higher than observed. We may need somewhat more compact aggregates, or different composition<sup>5</sup> (e.g., more silicate, see the right panel of Figure 8) to lower the peak polarization.

<sup>5</sup> The fact that the 100% silicate clusters have stronger negative polarization branches than the more absorptive silicate-graphite clusters is consistent with the findings by Zubko et al. (2009).

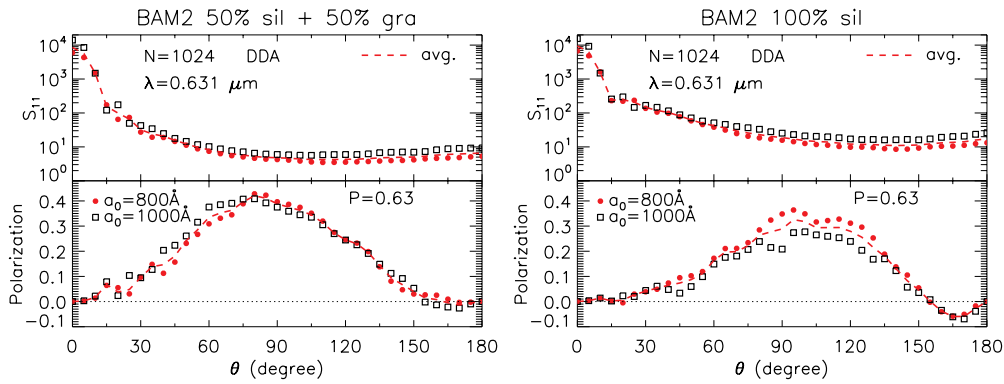


**Figure 8.** Scattering properties for aggregates resembling cometary dust (see text). For each composition we present results for  $N = 1024$  BAM2 clusters (three realizations, BAM2.1024.1-3, 54 orientations per realization) with monomer sizes  $a_0 = 0.08$  and  $0.1 \mu\text{m}$  ( $R = 1.12 \mu\text{m}$  and  $1.40 \mu\text{m}$ ). Dashed lines are for a size distribution  $dn/dR \propto R^{-3.5}$  for  $0.98 \mu\text{m} < R < 1.54 \mu\text{m}$ . Scattering properties are available at <http://www.astro.princeton.edu/~draine/SDJ2009.html>.

(A color version of this figure is available in the online journal.)

Alternatively, one may consider the mixture of fluffy aggregates and compact solid grains (e.g., Lasue et al. 2009). In their study, a larger fraction of porous BCCA aggregates is needed to produce a higher peak polarization for comet C/1995 O1 Hale-Bopp than for comet 1P/Halley, consistent with our argument that high porosity helps increase the polarization. Since only very porous BCCA clusters were used in their modeling, it will be interesting to see if our more compact BAM1 and BAM2 clusters will provide better fits for these comets in modeling the mixture of fluffy aggregates and compact solid grains. We note that, however, other types of irregular structures with sizes comparable to or larger than the incident wavelength are also capable of producing negative polarization branches (e.g., Zubko et al. 2006).

## 5. CONCLUSIONS

We have studied the phase function and linear polarization properties of light scattering by ballistic aggregates. We studied the wavelength dependence, cluster size dependence, and porosity dependence of the light scattering properties using the discrete-dipole-approximation, and compared with the EMT-Mie model. Our main conclusions are the following.

1. It is shown that though the EMT-Mie model reproduces similar trends in these dependences, it differs quantitatively from the DDA calculations. We recommend using DDA calculations if accurate results are desired.
2. Monomer size has negligible effects on the scattered light properties as long as monomers are small compared with the incident wavelength  $\lambda$ . Even when the monomers are no longer small (e.g.,  $2\pi a_0/\lambda \sim 1.6$ ), the monomer size appears to be of secondary importance for the phase function and polarization  $p(\theta)$ .
3. The phase function is mainly determined by  $R/\lambda$ ; increasing  $R/\lambda$  decreases the backscattering relative to forward scattering.
4. When  $R/\lambda \ll 1$  (e.g., in the Rayleigh limit), increasing  $R/\lambda$  decreases the polarization. For  $R \gtrsim \lambda$ , the dependence of polarization on  $R/\lambda$  depends on the dielectric function: for materials that are not strongly absorbing, increasing  $R/\lambda$  results in decreasing polarization, at least for  $R/\lambda \lesssim 2$  (e.g., Figures 7(c) and (d), showing 100% silicate BAM2 clusters at  $\lambda = 0.501 \mu\text{m}$  and  $0.631 \mu\text{m}$ ); however, at vacuum UV wavelengths where the materials are strongly absorbing, increasing  $R/\lambda$  can increase the polarization

(e.g., Figures 5(a) and (c), showing scattering at  $\lambda = 0.126 \mu\text{m}$ ).

5. The degree of polarization depends on the size parameter as well as porosity, but high porosity helps increase polarization in both the  $R \lesssim \lambda$  and  $R \gtrsim \lambda$  regimes.
6. We present aggregates with BAM2 geometry, moderate porosity  $\mathcal{P} \approx 0.6$ , and sub- $\mu\text{m}$  sizes which can reproduce the scattered light phase function and polarization observed in the AU Mic debris disk.
7. We present aggregate models with BAM2 geometry and moderate porosity  $\mathcal{P} \approx 0.6$  that can reproduce the albedo and polarization  $p(\theta)$  observed for cometary dust, including the negative polarization observed at scattering angles  $160^\circ \lesssim \theta < 180^\circ$ . These aggregates are composed of silicate and graphite, and are of  $\gtrsim \mu\text{m}$  size. Such moderately porous aggregates are promising candidates for cometary dust.

This research was supported in part by NSF grant AST 04-06883. Computations were performed on the Della and Artemis computer clusters at Princeton University.

## REFERENCES

- Bertini, I., Thomas, N., & Barbieri, C. 2007, *A&A*, **461**, 351  
 Blum, J., & Wurm, G. 2000, *Icarus*, **143**, 138  
 Bohren, C. F., & Huffman, D. R. 1983, *Absorption and Scattering of Light by Small Particles* (New York: Wiley)  
 Brownlee, D. E. 1985, *Annu. Rev. Earth Planet. Sci.*, **13**, 147  
 Chernova, G. P., Jockers, K., & Kiselev, N. N. 1996, *Icarus*, **121**, 38  
 Dartois, E., Muñoz Caro, G. M., Deboffle, D., & d'Hendecourt, L. 2004, *A&A*, **423**, L33  
 Dobrovolsky, O. V., Kiselev, N. N., & Chernova, G. P. 1986, *Earth Moon Planets*, **34**, 189  
 Dohnanyi, J. W. 1969, *J. Geophys. Res.*, **74**, 2531  
 Dollfus, A., Bastien, P., Le Borgne, J.-F., Lévassieur-Regourd, A. C., & Mukai, T. 1988, *A&A*, **206**, 348  
 Dorschner, J., & Henning, T. 1995, *A&AR*, **6**, 271  
 Draine, B. T. 2003, *ApJ*, **598**, 1017  
 Draine, B. T., & Flatau, P. 1994, *J. Opt. Soc. Am.*, **11**, 1491  
 Draine, B. T., & Flatau, P. 2008, <http://arXiv.org/abs/astro-ph/0809.0337>  
 Draine, B. T., & Lee, H. M. 1984, *ApJ*, **285**, 89  
 Eaton, N., Scarrott, S. M., & Gledhill, T. M. 1992, *MNRAS*, **258**, 384  
 Graham, J. R., Kalas, P. G., & Matthews, B. C. 2007, *ApJ*, **654**, 595  
 Hanner, M. S., & Newburn, R. L. 1989, *AJ*, **97**, 254  
 Henyey, L. G., & Greenstein, J. L. 1940, *Ann. Astrophys.*, **3**, 117  
 Kimura, H., Kolokolova, L., & Mann, I. 2006, *A&A*, **449**, 1243  
 Kiselev, N. N., Jockers, K., & Bonev, T. 2004, *Icarus*, **168**, 385  
 Kozasa, T., Blum, J., & Mukai, T. 1992, *A&A*, **263**, 423

- Kozasa, T., Blum, J., Okamoto, H., & Mukai, T. 1993, *A&A*, **276**, 278
- Krause, M., & Blum, J. 2004, *Phys. Rev. Lett.*, **93**, 021103
- Lasue, J., Levasseur-Regourd, A. C., Hadamcik, E., & Alcouffe, G. 2009, *Icarus*, **199**, 129
- Levasseur-Regourd, A. C., Hadamcik, E., & Renard, J. B. 1996, *A&A*, **313**, 327
- Levasseur-Regourd, A. C., & Hadamcik, E. 2001, in *ESA SP-495: Meteoroids 2001 Conference*, ed. B. Warmbein (Noordwijk: ESA), 587
- Lumme, K., & Rahola, J. 1994, *ApJ*, **425**, 653
- Mackowski, D. W. 1991, *Proc. R. Soc. A*, **433**, 599
- Mathis, J. S., Rumpl, W., & Nordsieck, K. H. 1977, *ApJ*, **217**, 425
- Mathis, J. S., & Whiffen, G. 1989, *ApJ*, **341**, 808
- Ossenkopf, V. 1993, *A&A*, **280**, 617
- Pendleton, Y. J., & Allamandola, L. J. 2002, *ApJS*, **138**, 75
- Petrova, E. V., Jockers, K., & Kiselev, N. N. 2000, *Icarus*, **148**, 526
- Purcell, E. M., & Pennypacker, C. R. 1973, *ApJ*, **186**, 705
- Rouleau, F., & Martin, P. G. 1991, *ApJ*, **377**, 526
- Shen, Y., Draine, B. T., & Johnson, E. T. 2008, *ApJ*, **689**, 260
- Tanaka, H., Inaba, S., & Nakazawa, K. 1996, *Icarus*, **123**, 450
- Warren, J. L., Barrett, R. A., Dodson, A. L., Watts, L. A., & Zolensky, M. E. 1994, *Cosmic Dust Catalog*, 14
- Weidenschilling, S. J. 1997, *Icarus*, **127**, 290
- West, R. A. 1991, *Appl. Opt.*, **30**, 5316
- Wurm, G., & Blum, J. 1998, *Icarus*, **132**, 125
- Xu, Y.-L. 1997, *Appl. Opt.*, **36**, 9496
- Zubko, E., Kimura, H., Shkuratov, Y., Muinonen, K., Yamamoto, T., Okamoto, H., & Videen, G. 2009, *J. Quant. Spectrosc. Radiat. Transf.*, in press
- Zubko, E., Shkuratov, Y., Kiselev, N. N., & Videen, G. 2006, *J. Quant. Spectrosc. Radiat. Transf.*, **101**, 416